Augmented Reality Visualization With Image Overlay for MRI-Guided Intervention: Accuracy for Lumbar Spinal Procedures With a 1.5-T MRI System

Jan Fritz[1]
Paweena U-Thainual[2,3]
Tamas Ungi[4]
Aaron J. Flammang[5]
Nathan B. Cho[2]
Gabor Fichtinger[4]
Iulian I. Iordachita[2]
John A. Carrino[1]

Keywords: augmented reality guidance, diskography, epidural injection, interventional MRI, MR-guided spine injection

DOI:10.2214/AJR.11.6918

Received March 21, 2011; accepted after revision June 22, 2011.

Supported by National Cancer Institute grant 1 R01 CA118371-01A2.

[1]Musculoskeletal Division, Russell H. Morgan Department of Radiology and Radiological Science, Johns Hopkins University School of Medicine, 601 N Caroline St, JHOC 5165, Baltimore, MD 21287. Address correspondence to J. A. Carrino (jcarrin2@jhmi.edu).

[2]Department of Mechanical Engineering and Laboratory for Computational Sensing and Robotics, Johns Hopkins University, Baltimore, MD.

[3]Department of Mechanical and Materials Engineering, Queens University, Kingston, ON, Canada.

[4]School of Computing, Queen's University, Kingston, ON, Canada.

[5]Siemens Corporate Research, Center for Applied Medical Imaging (CAMI), Baltimore, MD.

Supplemental Data
Available online at www.ajronline.org.

WEB
This is a Web exclusive article.

AJR 2012; 198:W266–W273

0361–803X/12/1983–W266

OBJECTIVE. The purpose of this study was to prospectively evaluate the accuracy of an augmented reality image overlay system in MRI-guided spinal injection procedures.

MATERIALS AND METHODS. An augmented reality prototype was used in conjunction with a 1.5-T MRI system. A human lumbar spine phantom was used in which 62 targets were punctured to assess the accuracy of the system. Sixty anatomic targets (facet joint, disk space, and spinal canal) were punctured to assess how the accuracy of the system translated into practice. A visualization software interface was used to compare planned needle paths and final needle locations on coregistered CT images (standard of reference). Outcome variables included entry error, angle error, depth error, target error, successful access of anatomic targets, number of needle adjustments, and time requirements.

RESULTS. Accuracy assessments showed entry error of 1.6 ± 0.8 mm, angle error of 1.6° ± 1.0°, depth error of 0.7 ± 0.5 mm, and target error of 1.9 ± 0.9 mm. All anatomic targets (60 of 60 insertions) were successfully punctured, including all 20 facet joints, all 20 disks, and all 20 spinal canals. Four needle adjustments (6.7%) were required. Planning of a single needle path required an average of 55 seconds. A single needle insertion required an average of 1 minute 27 seconds.

CONCLUSION. The augmented reality image overlay system evaluated facilitated accurate MRI guidance for successful spinal procedures in a lumbar spine model. It exhibited potential for simplifying the current practice of MRI-guided lumbar spinal injection procedures.

Spinal injections are widely performed, minimally invasive diagnostic and therapeutic procedures that often complement diagnostic imaging and electromyography and augment medical and physical therapies [1]. In 1999, 576,318 spinal injection procedures were performed in the United States [2]. The most commonly performed procedures are epidural injection, perineural injection, diskography, and facet joint injection [2]. Most spinal injection procedures are performed under conventional x-ray fluoroscopic and CT guidance. These techniques are highly accurate and allow time-effective procedures [1, 3] but have the inevitable disadvantage of patient and operator exposure to ionizing radiation and its associated health risks [1, 3–7].

Interventional MRI has the favorable attributes of cross-sectional imaging, unparalleled soft-tissue contrast, true multiplanar imaging capabilities, and the absence of ionizing radiation. Numerous techniques of a variety of MRI-guided spinal injection procedures have been described [2, 8–16]. Despite the favorable attributes, however, the availability of interventional MRI continues to be limited. Contributing factors are the limited availability of open and wide-bore MRI systems, limited access to the intervention site and targets, increased duration of procedures compared with fluoroscopic and CT procedures, cost, and the more complex aspects of MRI acquisition and mechanisms of instrument visualization [16–19].

In an attempt to overcome some of these barriers, we developed a low-cost augmented reality system that can be used for MRI guidance with almost any conventional MRI system [20, 21]. Virtual MRI guidance is accomplished by projecting cross-sectional MR images into the patient space, generating a hybrid view of reality and MR images [22]. With this system, a variety of spinal injection procedures appear possible. The purpose of this study was to prospectively evaluate the accuracy of an augmented reality image overlay system for MRI-guided spinal injection procedures.

Materials and Methods

System Description

An MRI-compatible, 2D augmented reality image overlay system prototype was used in conjunction with a 1.5-T MRI system (Magnetom Espree, Siemens Healthcare). The design and components are shown in Figure 1. The image overlay system is used for static MRI guidance through generation of an augmented reality view by simultaneous visualization of the target object and its previously acquired MR image. This setup was realized by projection and reflection of the previously acquired axial MR image from a liquid crystal display to the operator via a semitransparent mirror. With use of this optical path, the respective MR image appeared projected into the visible target object under the image overlay system in appropriate size and location [22] (Fig. 1C). The intersection of the projected image and the object was indicated by the laser.

Hardware calibration of the floor-mounted image overlay system and the MRI system was achieved by matching the axial plane of the image overlay system with the axial plane of the MRI system by use of a calibration phantom oriented perpendicularly to the table of the MRI system (Fig. 1B). The calibration phantom was placed on the table of the MRI system so that the axial laser plane of the MRI unit paralleled its front face. Through table translation, the phantom was moved into the axial laser plane of the image overlay system. The image overlay system itself was then manually adjusted so that its laser paralleled the front face of the phantom.

The distance between the isocenter of the bore and the laser plane of the image overlay system was determined with the table position display of the MRI system. This value was used to calculate the absolute table positions necessary to translate the target object under the image overlay system in an appropriate location to match the respective MR image containing a target structure.

The virtual needle paths were planned on previously acquired MR images of the target object with the Perk Station module (version 7088) of the 3D Slicer software (version 3.6, 3D Slicer) [22–24] (Fig. 2A). The respective MR image with the virtual needle path was projected with the image overlay system into the target object in the appropriate location. The target was punctured by maneuvering of the needle along the virtual needle path (Fig. 2B).

Phantom

We used a human lumbar spine phantom consisting of five lumbar vertebral bodies and foam disks. The 67-year-old donor had a living diagnosis of spinal stenosis. The average height of the posterolateral disk spaces was 4.8 ± 0.5 mm (range, 4.1–5.1 mm; coefficient of variation (CV), 3.8%). The average center width and center height of the interlaminar spaces were 4.3 ± 0.7 mm (range, 3.7–5.3 mm; CV, 3.0%) and 5.7 ± 1.0 mm (range, 4.9–7.1 mm; CV, 1.6%). The average posterior width of the facet joint cavities was 0.7 ± 0.1 mm (range, 0.6–0.9 mm; CV, 10.4%). Mild posterior hypertrophic facet joint changes were present.

The phantom was placed on a foam bed and harbored in a 100 × 200 mm acrylic enclosure, which was embedded into a nontransparent animal protein gel (Sim-Test, Corbin) emulating the thickness and consistency of muscle tissue. The gel was additionally covered with a 0.6-mm-thick neoprene layer simulating skin. The flexible properties of the gel and neoprene layer avoided visible needle tracks. Several fiducial markers (MultiModality Fiducial Marker, IZI Medical Products) were placed on the surface of the phantom as reference points for software calibration and coregistration of MR and CT images.

Research Plan

The study consisted of two consecutive parts. We designed the first part to quantify the margin of error of the system (accuracy). We defined accuracy as the degree of closeness a needle tip can be placed to its previously defined target, thereby simulating typical needle trajectories and needle depths of lumbar spinal procedures. To avoid the introduction of bias secondary to contact with bone, we purposely chose targets without potential osseous contact, thereby targeting spinal nerve areas and periarticular facet joint areas. In the second part of the study, we sought to assess the efficacy of the system, defined as the ability of the operator to navigate a needle tip into a typical anatomic target. To receive a binary outcome (success versus failure), we selected anatomic structures with osseous boundaries, including the facet joint cavity, disk space, and spinal canal.

All targets were prospectively, randomly, and evenly assigned with a computer algorithm. The targets were specified by laterality and level on a printed list, with which the operator was provided before each series. The operator used the dominant and nondominant hands for needle insertions in an equal number of cases.

Accuracy—Sixty-two needle placements were planned. Thirty-one (50%) targets were located near the exit of the spinal nerves at the level of the neural foramina, simulating the needle placement for perineural spinal nerve injections. Thirty-one (50%) targets were posterior to the facet joints, simulating the needle placement for periarticular facet joint injections. Needle placements were performed in four series (n = 14, n = 16, n = 16, n = 16) related to the maximum numbers of four paired (eight) facet joints and four paired (eight) spinal nerves of the lumbar spine phantom. Needles were placed in a single attempt without further adjustments.

Efficacy—Sixty needle placements were planned. Twenty (33.3%) targets were the intervertebral space, simulating the puncture of disks for sampling or diskography; 20 were the facet joint cavity, simulating needle placement for intraarticular facet joint injections; and 20 were the posterior aspect of the spinal canal, simulating needle placement for epidural injections. Needle placements were performed in five series of 12 placements each, related to the maximum numbers of four intervertebral spaces and four interlaminar spaces for access to the spinal canal. In addition to using image overlay system guidance, the operator used tactile feedback during needle guidance.

Workflow

Initially, isotropic MR images of the entire phantom were acquired with a 3D sampling perfection with application optimized contrasts using different flip-angle evolutions (SPACE) sequence with T1-weighted prepared inversion recovery (TR/TE, 1100/34; inversion time, 835 ms; flip angle, 120°; number of signals averaged, 2; echo-train length, 41; slice thickness, 1 mm; number of slices, 100; FOV, 256 × 224 mm; base resolution, 256 pixels; phase resolution, 100%; bandwidth, 751 Hz; acquisition time, 14 minutes) and a flexible loop-shaped radiofrequency coil with a diameter of 16 cm. The MR volume was subsequently imported into the Perk Station software.

The operator used the Perk Station software to calibrate the image overlay system by aligning the overlay projection with the operator's line of sight on each side of the object. The operator then used the software to identify all previously defined targets and respective skin entry points on the imported MR images (Fig. 2A) and to calculate and display the respective needle path and insertion depth.

For each needle insertion, the operator moved the table of the MRI system to the calculated table position. MR-compatible, 22-gauge needles (Lufkin Needle, EZ-EM) 5, 10, and 15 cm long were used according to the length of the needle path. Individually adjustable depth markers affixed to the needle were used for guidance of the insertion depths.

Needle placement was performed under augmented reality MRI guidance. By looking through the semitransparent mirror, the operator simultaneously visualized the target object and its previously acquired MR image, including the virtual needle path (Fig. 2B). The operator identified the surface entry point as the intersection of the image overlay system laser and the displayed virtual needle path. To make the puncture, the operator

maneuvered the needle along the virtual needle path displayed through the semitransparent mirror (Fig. 2B).

After each needle was placed (intervertebral space, facet joint, spinal canal), axial proton density–weighted turbo spin-echo MR images (TR/TE, 11,442/12; flip angle, 120°; number of signals averaged, 1; echo-train length, 17; slice thickness, 3 mm; number of slices, 54; FOV, 256 × 224 mm; base resolution, 320 pixels; phase resolution, 100%; bandwidth, 252 Hz; acquisition time, 2.5 minutes) were obtained of the entire phantom for visual assessment of needle tip locations (success versus failure). After performing a visual inspection, the operator made optional needle adjustments and acquired final proton density–weighted turbo spin-echo images.

After all needles of the series were in satisfactory locations, the initial 3D SPACE sequence was repeated. Afterward, the board of the MRI table (Angio-MR Miyabi, Siemens Healthcare) was translated to an attached flat panel detector angiography system (Axiom Artis DFA, Siemens Healthcare), and a radiographic dataset (acquisition time, 20 seconds; tube voltage, 71 kVp; tube current, 278 mAs; rotation angle, 217°; number of images, 543; increment, 0.4°) was acquired. Preset computed correction for beam hardening, ring artifacts, and scattered radiation (DynaCT, Siemens Healthcare) was applied. An isotropic CT dataset (matrix size, 512 × 512; FOV, 180 × 180 mm, approximate voxel size, 0.4 mm) was reconstructed at a workstation (MMWP, Siemens Healthcare) with the bone smooth reconstruction kernel. DynaCT images and the final 3D SPACE MR images were fused by use of the 3D Slicer software.

Assessment of Outcome Variables

DynaCT images served as the standard of reference of the true needle tip location. Image fusion was performed to accurately localize the needles, because needle location tends to vary on MR images [25].

Accuracy—The Perk Station software was used for assessment of errors by comparison of planned needle paths and the true needle location as indicated by the needle artifact on DynaCT images. An operator outlined the true needle path by selecting and manually clicking on the skin entry point and tip of the needle.

The following parameters were assessed: length of needle paths; angle of needle paths relative to the patient's *y*-axis (0° reference); rate of accurate targeting of structures as indicated on the lists provided before each series; quality of fusion of MR and DynaCT images, which was assessed by two operators independently, who thereby assessed the congruence of osseous contours and needle artifacts (quality of fusion was categorized as excellent, good, or poor); total entry error, defined as the euclidean distance of the planned and actual skin entry points; angle error, defined as the included angle of the planned and actual needle paths; depth error, defined as the distance between the target locations and the needle tips along the needle trajectory; and target error, defined as the euclidean distance of the planned and actual position of the needle tips.

Efficacy—The rate of successful puncture of anatomic targets was assessed on DynaCT images (success versus failure) by comparison of the planned needle path with the true needle position. The operator's intraprocedural assessment of the final needle tip location was compared with the true needle tip location and categorized as accurate or inaccurate. The number and category of needle adjustments were assessed. Categories included needle relocation, defined as change of the needle trajectory; needle advancement; and needle withdrawal. Two readers blinded to series number, date, and time performed qualitative assessments independently and randomly. Images were assessed at a PACS workstation. During software calibration, planning, and needle insertion for all series, a team member recorded the time requirements during experiments.

Statistical and Quantitative Assessments

Statistical analysis was performed with a statistical software package (JMP version 7.01, SAS Institute). A value of $p < 0.05$ indicated a statistically significant difference. Quantitative variables were expressed as mean ± first SD and minimum and maximum values. Categoric variables were expressed as frequency and percentage.

Sample size was estimated with previously collected laboratory data with a total targeting error of 4.67 ± 1.94 mm according to the following formula: $n = 4\sigma^2(Z_{crit})^2/D^2$, where n is the sample size of the single study group; σ, the assumed SD for the group (1.94 mm); Z_{crit}, the standard normal deviation (1.96 for a significance criterion of 0.05); and D, the total width of the 95% CI (1 mm) [26]. A sample size minimum of 58 needle insertions was calculated to estimate the error of needle tip position within a 95% CI of ± 0.5 mm.

A vector space model was used to calculate entry, angle, depth, and target errors and their components. Measurements on images were performed three times by a single operator. Intrarater variability was assessed by use of coefficient of variation (CV) as CV = σ/μ, where σ is the first SD and μ is the arithmetic mean.

One-way analysis of variance with Tukey-Kramer post hoc testing and Kruskal-Wallis, Wilcoxon, and Student *t* tests were used to compute group differences. Learning curves were evaluated with curve-fitting statistics based on the Marquardt-Levenberg algorithm for approximation of the type of regression and calculation of regression coefficients and significance levels. The influence of angle and depth of needle path, entry error, and angle error on target error was tested by multivariate linear regression analysis with a backward stepwise approach.

Results

Accuracy

The average length of the needle path was 36.7 ± 9.9 mm (range, 23.1–53.0 mm). The average axial angle of the needle path was 13.6° ± 9.6° (range, 0–32.3°). There were no significant differences between series. All 62 targets were accurately selected (Fig. 2). The quality of image fusions was excellent for all four image volumes. There was no disagreement between observers. Entry, angle, depth, and target errors are shown in Table 1. Errors were not significantly different in comparisons of periarticular facet joint and spinal nerve targets.

Entry error was significantly different among the four series ($p \leq 0.001$), whereas angle error, depth error, and target error were not significantly different ($p = 0.395$, $p = 0.447$, $p = 0.679$). The results of analyses of entry error ($r = 0.55$, $p \leq 0.0001$) and target error ($r = 0.213$, $p = 0.038$) indicated a significant learning curve. Angle error ($r = 0.23$, $p = 0.566$) and depth error ($r = 0.137$, $p = 0.569$) were not associated with a learning curve

TABLE 1: Summary of Entry, Angle, Target, and Depth Errors

Target	Entry Error (mm)[a]	Angle Error (°)[b]	Target Error (mm)[c]	Depth Error (mm)[d]
All (*n* = 62)	1.6 ± 0.8 (0.2–3.1)	1.6 ± 1.0 (0.1–3.5)	1.9 ± 0.9 (0.4–4.1)	0.7 ± 0.5 (0–2.4)
Facet joints (*n* = 31)	1.5 ± 0.7 (0.6–3.1)	1.7 ± 0.9 (0.3–3.5)	1.9 ± 0.9 (0.4–4.0)	0.8 ± 0.6 (0–2.4)
Spinal nerves (*n* = 31)	1.6 ± 0.8 (0.2–3.0)	1.5 ± 1.0 (0.1–3.4)	2.0 ± 0.9 (0.5–4.1)	0.6 ± 0.4 (0–1.6)

Note—Values in parentheses are ranges.
[a]Coefficient of variation, 8.4% ± 9.0% (0.4–46.6%).
[b]Coefficient of variation, 22.9% ± 17.4% (2.0–77.0%).
[c]Coefficient of variation, 7.5% ± 6.3% (0.6–28.4%).
[d]Coefficient of variation, 28.5% ± 22.8% (2.0–95.3%).

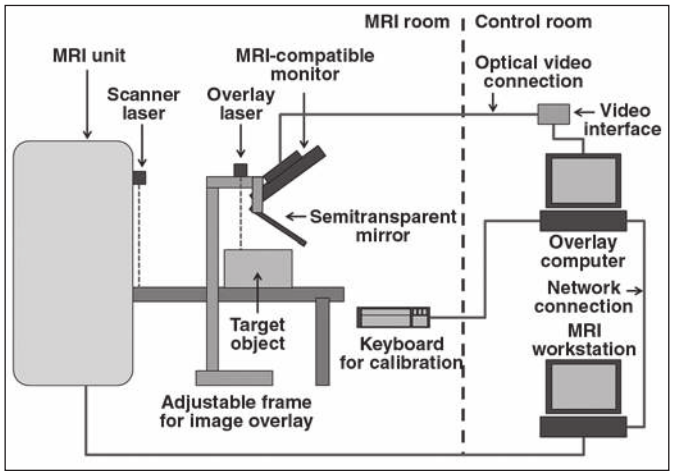

A

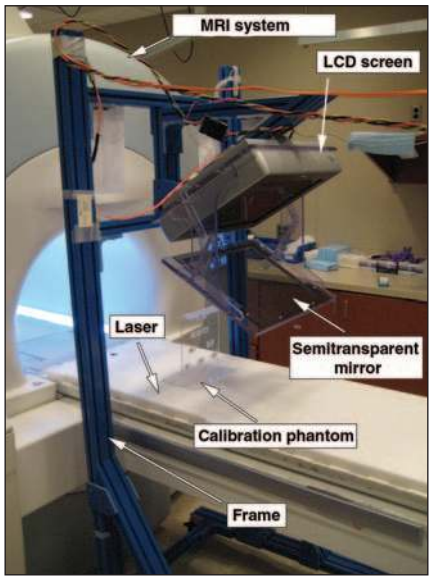

B

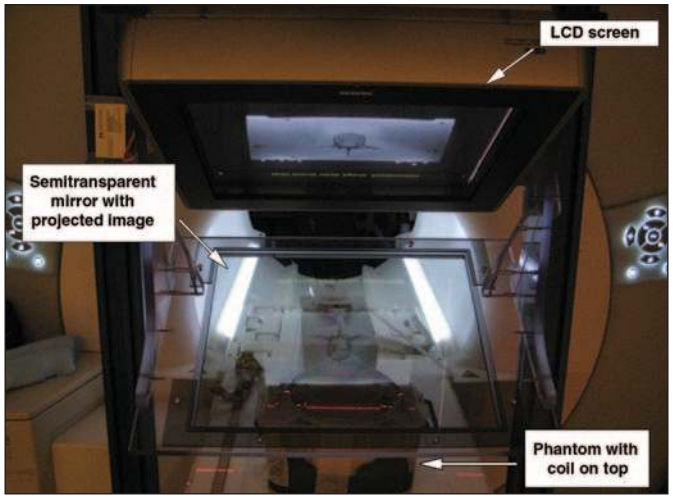

C

Fig. 1—Image overlay augmented reality system used in conjunction with clinical 1.5-T MRI system. LCD = liquid crystal display.
A, Schematic shows system components and interconnections.
B, Photograph shows mounted image overlay system and MRI unit.
C, Photograph shows MR image and reality. Intersection of projected image and object is marked with laser.

(Fig. 3). Entry error and angle error were the only variables with a significant effect on target error ($p \leq 0.001$, $p = 0.008$). The effects of depth and angle of the needle path were not significant ($p = 0.122$, $p = 0.095$).

Efficacy

All 60 anatomic targets were successfully punctured, including disks (Fig. 4), facet joints (Fig. 5), and virtual epidural spaces (Fig. 6). (Figs. S4A–S6A, supplemental video clips, can be viewed from the information box in the upper right corner of this article.) There was no disagreement between observers. After operator assessment of proton density–weighted turbo spin-echo MR images, four needle adjustments (4/60, 6.7%) were performed, including one needle relocation and three needle advancements. The final operator assessment of proton density–weighted turbo spin-echo images was concordant with confirmatory DynaCT findings in all targets. There was no disagreement between observers. Software calibration required an average of 6.4 ± 1.5 minutes (range, 5–10 minutes). The planning phase required an average of 12.1 ± 3.1 minutes (range, 8–16 minutes). The needle insertion phase required an average of 19.7 ± 3.3 minutes (range, 16–26 minutes). Planning of a single needle path required an average of 55 seconds. Insertion of a single needle required an average of 1 minute 27 seconds.

Discussion

Our investigation showed that the augmented reality image overlay system evaluated is sufficiently accurate for successful puncture of even small lumbar targets, such as the facet joints. The overall target error was 1.9 ± 0.9 mm. All anatomic targets were successfully punctured, requiring a total of four needle adjustments. The needle tip location was accurately assessed on intraprocedural proton density–weighted turbo spin-echo MR images.

Performing MRI-guided lumbar spinal procedures with the image overlay system overcomes two fundamental limitations of interventional MRI, namely, the requirement of a dedicated open or wide-bore MRI system and limited patient access inside the bore [17–19, 27]. The image overlay system can be used with any MRI system with horizontal patient orientation and an encoded table, especially with conventional closed-bore MRI systems in which no direct patient

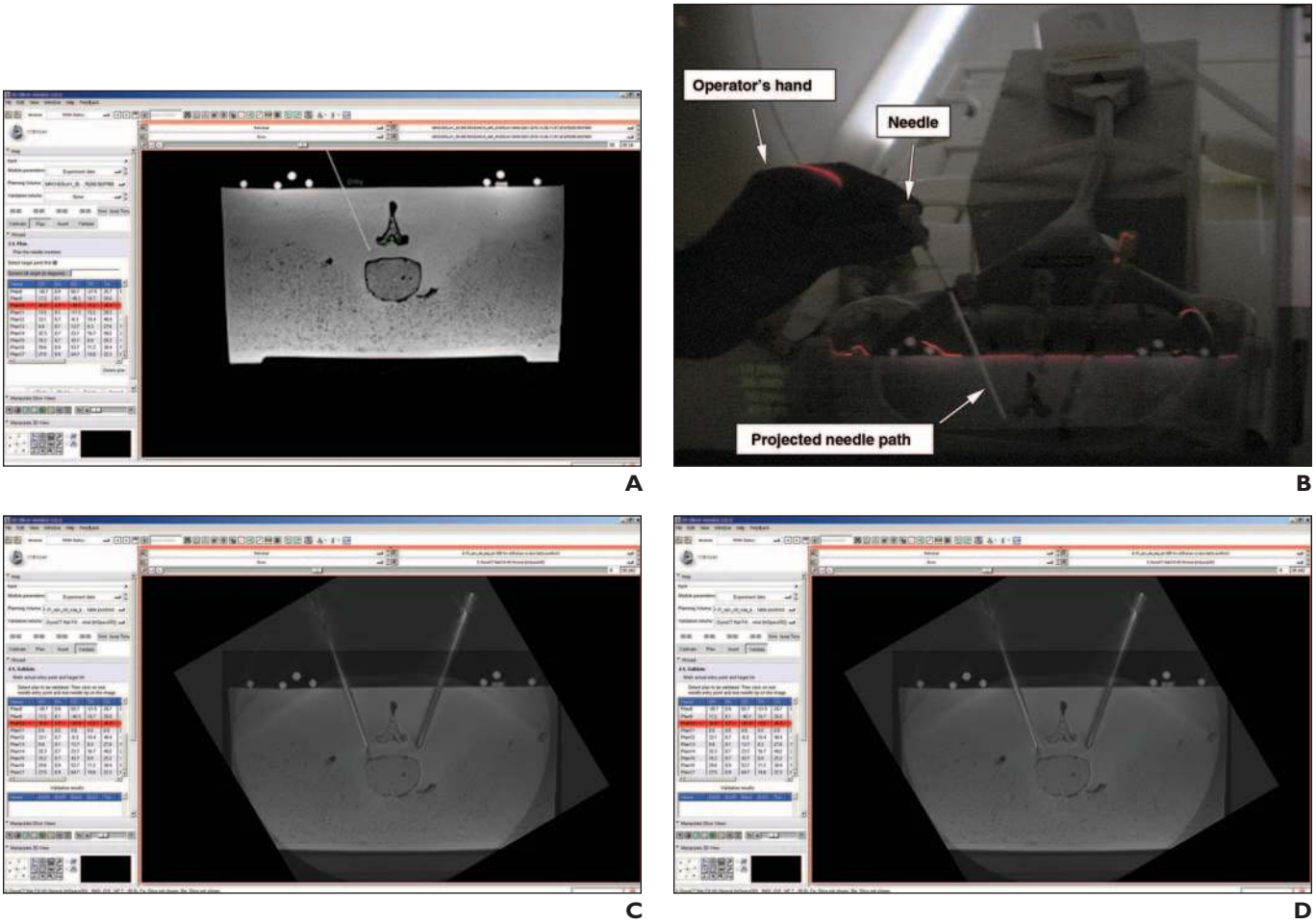

Fig. 2—Assessment of accuracy.
A, Screen shot shows planning of needle path simulating perineural injection. Planned needle path is indicated by line connecting Target and Entry.
B, Photograph shows needle insertion and projected MR image with needle path trajectory guide.
C, Screen shot shows image fusion. Fused T1-weighted MR and DynaCT (Siemens Healthcare) images show MRI and CT needle artifacts.
D, Screen shot shows verified needle path and location of needle tip with Perk Station software (3D Slicer). Yellow line shows planned needle path.

access is possible. Use of the image overlay system not only obviates patient access inside the bore but also allows individually adjustable patient access. The height of the unit containing the semitransparent mirror is adjustable and can be adapted to procedure- and patient-specific space requirements. This configuration contrasts to that previously reported for interventional MRI, in which needle placement was performed inside the bore of an open or wide-bore MRI system [9, 10, 12–15, 18, 28].

The definition of an augmented reality system is based on simultaneous visualization of medical images and a target [29]. The combination of MR image, target, and tactile feedback during needle placement creates a look-and-feel ambiance and thus simplifies MRI-guided intervention. That the targeted structure appears in the actual location of the patient's body results in intuitive hand-eye coordination unlike the spatial and visual separation of the intervention site and MR image display of interventional MRI inside the bore, which requires the interventionalist to mentally transfer the image information onto the patient [10, 11, 14, 17–19, 21, 27]. With the image overlay system, no additional visualization devices, such as a head-mounted display, are required [30].

The image overlay system was designed with low cost in mind. Currently, the cost of the system prototype adds as much as $13,000, mostly related to the shielded monitor (≈$10,000). However, if the configuration of the MRI system allows constant location of the image overlay system outside the 5-gauss zone, unshielded conventional liquid crystal display can be used, decreasing the cost of the entire system to approximately $4000.

The image overlay system allows the use of high-resolution MRI, which combines the advantage of superior soft-tissue contrast and depiction of small structures. For instance, it improves assessment of the frequently variable shape and orientation of the facet joint space, which results in more appropriately oriented needle paths and subsequent easier joint access. Without the image overlay system, high-resolution MRI used to be impractical for direct MRI guidance because of the requirement for either repetitive or real-time image acquisition.

Even though the acquisition time for a high-resolution planning volume requires considerable time, the overall procedure time is expected to be substantially less, because only a single preinterventional planning volume is required. Depending on the magnitude of this volume, multiple anatomic levels can be

successively targeted. Although the acquisition time for the MRI planning volume in our study was 14 minutes, related to the coverage of five vertebral bodies, image acquisition of a single lumbar level, for example in patients, will be proportionally shorter.

By using DynaCT images as the reference standard, we found that needle locations can be accurately assessed on rapidly acquired proton density–weighted turbo spin-echo images. With this sequence, a volume of the size of a vertebral body can be imaged in 15–30 seconds, which will more than likely shorten the duration of MRI-guided interventions in a closed-bore MRI unit.

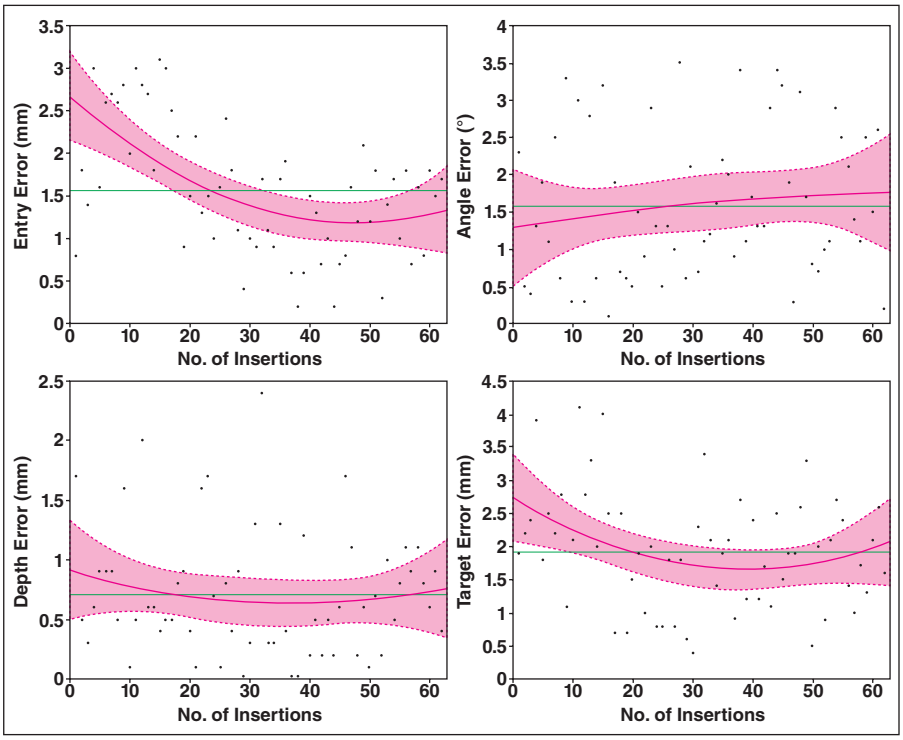

Fig. 3—Scatterplots show entry error, angle error, depth error, and target error and results of curve estimation regression analysis. Analysis of entry error ($r = 0.52$, $p \leq 0.0001$) and target error ($r = 0.213$, $p = 0.038$) showed significant learning curve, but analysis of angle error ($r = 0.23$, $p = 0.445$) and depth error ($r = 0.137$, $p = 0.569$) showed no evidence of learning curve. Pink indicates 95% confidence band.

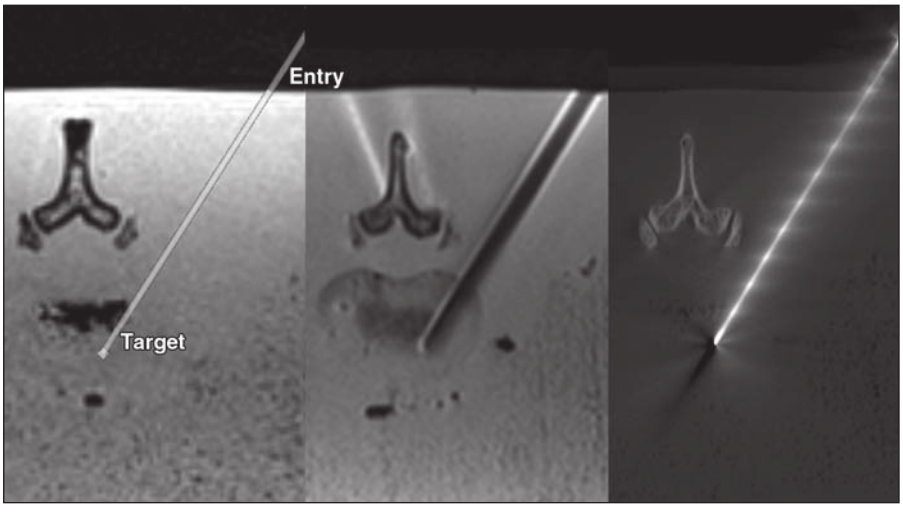

Fig. 4—Sequence of simulated disk puncture. T1-weighted axial MR image (*left*) obtained with Perk Station software (3D Slicer) shows planning of needle path. Proton density–weighted MR image (*center*) shows needle verification immediately after placement. Final DynaCT (Siemens Healthcare) image (*right*) shows proof of needle location. See also Figure S4A, video clip, in supplemental data online.

Factors contributing to the target error of 1.9 mm include technical and operator-dependent factors. Regression analysis revealed entry error and angle error as major contributors. Although entry error decreased substantially with training, angle error remained almost constant over time. Entry error is further influenced by the technical boundaries of the image overlay system and by the measurement resolution, which include the thickness of the image overlay system laser (≈1 mm), voxel size of the projected image (1 × 1 × 1 mm in our study), and small variations of the absolute table position of the MRI system. Small angle errors are additionally related to small inhomogeneities of the semitransparent mirror. Furthermore, the static nature of the image overlay system requires an individually adjustable needle depth guide, which is included in most commercially available MRI-compatible needles. Although continuous monitoring of the needle tip is not possible with the image overlay system, the overall depth error of 0.7 mm did not require needle adjustments in most cases.

Because the meaning of an overall target error of 1.9 mm can be difficult to translate into practice, we tested the operator's ability to puncture frequently targeted spinal structures. Our finding of a success rate of 100% suggests that the accuracy of the system is sufficient for lumbar spinal injection procedures. Even facet joints, which have been found to be challenging in clinical interventional MRI, can be reliably accessed with the image overlay system [10].

Our results show that augmented reality can be highly accurate. This finding is in accordance with published data on a dynamic head-mounted augmented reality system for MRI guidance that had a mean error of 1.1 mm, allowing differences in the method of error assessment [30]. Previous studies of different guidance techniques showed target error of 3.1–7.5 mm with stereotactic optical guidance [31] and 3.0 mm with a custom-made manipulator [32], a root mean square error of 2.6–4.8 mm with a robotic system [33], a target accuracy of 3.2 mm with an MRI-compatible manipulator system [34], and needle displacement error of 2.2–3.9 mm with a table-mounted reference system [35].

Although the results are encouraging, our study had several limitations. The mild

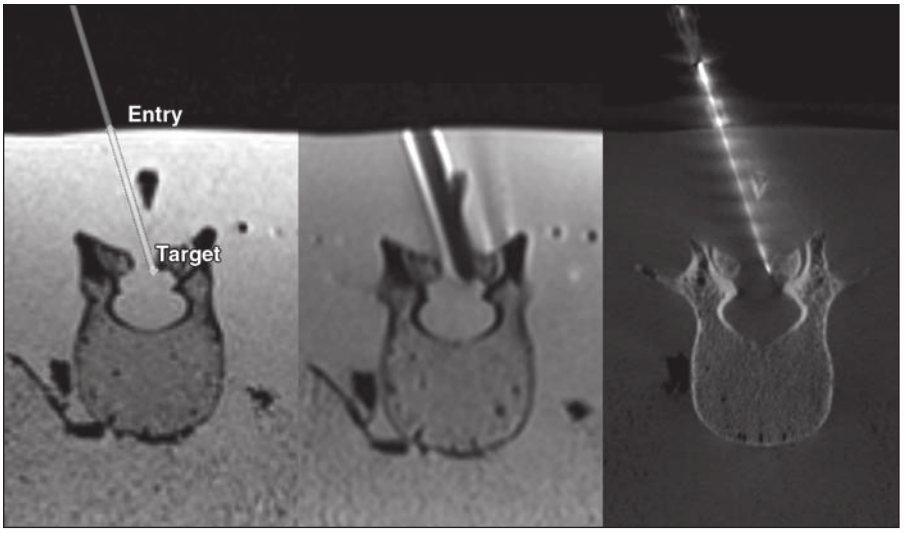

Fig. 6—Sequence of simulated epidural puncture. T1-weighted axial MR image (*left*) obtained with Perk Station software (3D Slicer) shows planning of needle path. Proton density–weighted MR image (*center*) needle verification immediately after placement. Final DynaCT (Siemens Healthcare) image (*right*) shows proof of needle location. See also Figure S6A, video clip, in supplemental data online.

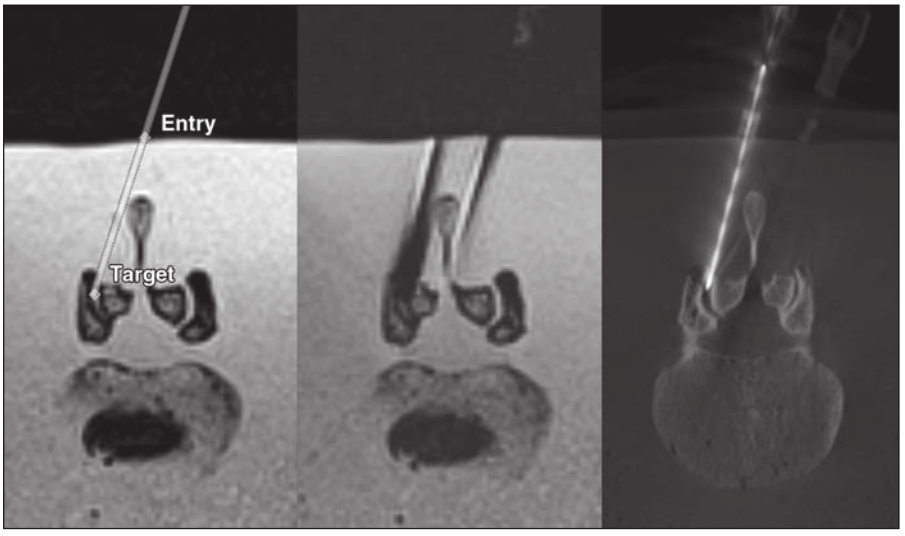

Fig. 5—Sequence of simulated facet joint puncture. T1-weighted axial MR image (*left*) obtained with Perk Station software (3D Slicer) shows planning of needle path. Proton density–weighted MR image (*center*) shows needle verification immediately after placement. Final DynaCT (Siemens Healthcare) image (*right*) shows proof of needle location. See also Figure S5A, video clip, in supplemental data online.

hypertrophic facet joint changes of our phantom might have been less severe than those encountered in typical patient populations. Multiple measurements were obtained in the same phantom, which might have introduced learning bias. However, because each series required new system calibration, repositioning of the phantom, and acquisition of a new image volume, levels and orientations of the needle paths differed substantially, and learning curve bias seems unlikely. Influences of patient and respiratory motion were not present, and these elements can have a substantial influence on accuracy, especially when an augmented reality system is used. We will extend our work to assess the efficacy of the system for spinal injection procedures in a cadaveric trial and the effectiveness in a clinical trial.

On the basis of the results of this investigation, we conclude that the augmented reality image overlay system evaluated is sufficiently accurate for successful MRI-guided lumbar spinal injection procedures. We believe use of the system can simplify the current practice of these procedures. Development of this system may contribute to wider availability of MRI guidance, especially in the care of adolescents and pregnant women, who should avoid radiation exposure at any cost.

Acknowledgment

We thank John Eng for assistance in sample size calculation.

References

1. Fritz J, Niemeyer T, Clasen S, et al. Management of chronic low back pain: rationales, principles, and targets of imaging-guided spinal injections. *RadioGraphics* 2007; 27:1751–1771
2. Carrino JA, Morrison WB, Parker L, Schweitzer ME, Levin DC, Sunshine JH. Spinal injection procedures: volume, provider distribution, and reimbursement in the U.S. medicare population from 1993 to 1999. *Radiology* 2002; 225:723–729
3. Wagner AL. Selective lumbar nerve root blocks with CT fluoroscopic guidance: technique, results, procedure time, and radiation dose. *AJNR* 2004; 25:1592–1594
4. Krombach GA, Schmitz-Rode T, Wein BB, et al. Potential of a new laser target system for percutaneous CT-guided nerve blocks: technical note. *Neuroradiology* 2000; 42:838–841
5. Nawfel RD, Judy PF, Silverman SG, Hooton S, Tuncali K, Adams DF. Patient and personnel exposure during CT fluoroscopy-guided interventional procedures. *Radiology* 2000; 216:180–184
6. Paulson EK, Sheafor DH, Enterline DS, McAdams HP, Yoshizumi TT. CT fluoroscopy–guided interventional procedures: techniques and radiation dose to radiologists. *Radiology* 2001; 220:161–167
7. Wagner LK. CT fluoroscopy: another advancement with additional challenges in radiation management. *Radiology* 2000; 216:9–10
8. Blanco Sequeiros R, Carrino JA. Musculoskeletal interventional MR imaging. *Magn Reson Imaging Clin N Am* 2005; 13:519–532
9. Fritz J, Henes JC, Thomas C, et al. Diagnostic and interventional MRI of the sacroiliac joints using a 1.5-T open-bore magnet: a one-stop-shopping approach. *AJR* 2008; 191:1717–1724
10. Fritz J, Clasen S, Boss A, et al. Real-time MR fluoroscopy-navigated lumbar facet joint injections: feasibility and technical properties. *Eur Radiol* 2008; 18:1513–1518
11. Fritz J, Thomas C, Tzaribachev N, et al. MRI-guided injection procedures of the temporomandibular joints in children and adults: technique, accuracy, and safety. *AJR* 2009; 193:1148–1154
12. Fritz J, Thomas C, Clasen S, Claussen CD, Lewin JS, Pereira PL. Freehand real-time MRI-guided lumbar spinal injection procedures at 1.5 T: feasi-

bility, accuracy, and safety. *AJR* 2009; 192:11-7; [web]W161–W167

13. Fritz J, Tzaribachev N, Thomas C, et al. Evaluation of MR imaging guided steroid injection of the sacroiliac joints for the treatment of children with refractory enthesitis-related arthritis. *Eur Radiol* 2011; 21:1050–1057
14. Ojala R, Vahala E, Karppinen J, et al. Nerve root infiltration of the first sacral root with MRI guidance. *J Magn Reson Imaging* 2000; 12:556–561
15. Ojala R, Klemola R, Karppinen J, Sequeiros RB, Tervonen O. Sacro-iliac joint arthrography in low back pain: feasibility of MRI guidance. *Eur J Radiol* 2001; 40:236–239
16. Smith KA, Carrino J. MRI-guided interventions of the musculoskeletal system. *J Magn Reson Imaging* 2008; 27:339–346
17. Hushek SG, Martin AJ, Steckner M, Bosak E, Debbins J, Kucharzyk W. MR systems for MRI-guided interventions. *J Magn Reson Imaging* 2008; 27:253–266
18. Lewin JS, Petersilge CA, Hatem SF, et al. Interactive MR imaging-guided biopsy and aspiration with a modified clinical C-arm system. *AJR* 1998; 170:1593–1601
19. Weiss CR, Nour SG, Lewin JS. MR-guided biopsy: a review of current techniques and applications. *J Magn Reson Imaging* 2008; 27:311–325
20. Weiss CR, Marker DR, Fischer GS, Fichtinger G, Machado AJ, Carrino JA. Augmented reality visualization using image-overlay for MR-guided interventions: system description, feasibility, and initial evaluation in a spine phantom. *AJR* 2011; 196:653; [web]W305–W307
21. Fischer GS, Deguet A, Schlattman D, et al. MRI image overlay: applications to arthrography needle insertion. *Stud Health Technol Inform* 2006; 119:150–155
22. Fichtinger G, Deguet A, Masamune K, et al. Image overlay guidance for needle insertion in CT scanner. *IEEE Trans Biomed Eng* 2005; 52:1415–1424
23. Vikal S, Thainual P, Carrino JA, Iordachita I, Fischer GS, Fichtinger G. Perk Station: percutaneous surgery training and performance measurement platform. *Comput Med Imaging Graph* 2010; 34:19–32
24. Gering DT, Nabavi A, Kikinis R, et al. An integrated visualization system for surgical planning and guidance using image fusion and an open MR. *J Magn Reson Imaging* 2001; 13:967–975
25. Lewin JS, Duerk JL, Jain VR, Petersilge CA, Chao CP, Haaga JR. Needle localization in MR-guided biopsy and aspiration: effects of field strength, sequence design, and magnetic field orientation. *AJR* 1996; 166:1337–1345
26. Eng J. Sample size estimation: how many individuals should be studied? *Radiology* 2003; 227:309–313
27. Fritz J, Pereira PL. MR-guided pain therapy: principles and clinical applications [in German] *Rofo* 2007; 179:914–924
28. Streitparth F, Walter T, Wonneberger U, et al. Image-guided spinal injection procedures in open high-field MRI with vertical field orientation: feasibility and technical features. *Eur Radiol* 2010; 20:395–403
29. Moche M, Trampel R, Kahn T, Busse H. Navigation concepts for MR image-guided interventions. *J Magn Reson Imaging* 2008; 27:276–291
30. Wacker FK, Vogt S, Khamene A, et al. An augmented reality system for MR image-guided needle biopsy: initial results in a swine model. *Radiology* 2006; 238:497–504
31. Silverman SG, Collick BD, Figueira MR, et al. Interactive MR-guided biopsy in an open-configuration MR imaging system. *Radiology* 1995; 197:175–181
32. Hata N, Tokuda J, Hurwitz S, Morikawa S. MRI-compatible manipulator with remote-center-of-motion control. *J Magn Reson Imaging* 2008; 27:1130–1138
33. Tokuda J, Fischer GS, Csoma C, et al. Software strategy for robotic transperineal prostate therapy in closed-bore MRI. *Med Image Comput Comput Assist Interv* 2008; 11:701–709
34. Christoforou E, Akbudak E, Ozcan A, Karanikolas M, Tsekos NV. Performance of interventions with manipulator-driven real-time MR guidance: implementation and initial in vitro tests. *Magn Reson Imaging* 2007; 25:69–77
35. Busse H, Garnov N, Thormer G, et al. Flexible add-on solution for MR image-guided interventions in a closed-bore scanner environment. *Magn Reson Med* 2010; 64:922–928

FOR YOUR INFORMATION

The data supplement accompanying this Web exclusive article can be viewed from the information box in the upper right corner of the article at: www.ajronline.org.